Trends in Computational and Applied Mathematics, **27** (2026), e01901
Sociedade Brasileira de Matemática Aplicada e Computacional
Online version ISSN 2676-0029 www.scielo.br/tcam
ORIGINAL ARTICLE
doi: 10.5540/tcam.2026.027.e01901

Tuned Liquid Column Dampers under Stochastic Excitation with Viscosity and Geometric Effects

M. O. SILVA[1*], J. O. MAUPRIVEZ[2], F. L. C. SILVA[3],
B. C. CAYRES[4] and D. C. GUERRIERI[4]

Received on December 11, 2025 / Accepted on August 23, 2026

ABSTRACT. Tuned Liquid Column Dampers (TLCDs) are recognized for their effectiveness in passive vibration control. However, accurately modeling their damping characteristics remains a challenge due to the complex, nonlinear dependence of head loss on fluid properties and flow regimes. This study presents a numerical framework to evaluate the dynamic response of a primary structure coupled with a TLCD under stochastic excitation, to assess the TLCD's effectiveness in passive vibration control. Unlike traditional approaches that assume a constant experimental damping coefficient, this work employs a phenomenological model that dynamically evaluates the instantaneous head loss using fundamental fluid mechanics principles, employing the Poiseuille and Swamee-Jain formulations for laminar and turbulent regimes, respectively. The resulting system of stiff, nonlinear differential equations is solved using the Backward Differentiation Formula (BDF) method. A comparative analysis of four working fluids (water, ethylene glycol, SAE 30 oil, and glycerin) was conducted to investigate the impact of viscosity on efficiency. For the chosen standard configuration, with a small-diameter tube setup ($D \approx 21$ mm), the results indicate that simply substituting water with high-viscosity fluids increases the simulated structural response. Furthermore, a refined parametric search varying the liquid column length (L) and tube diameter (D) generated performance heatmaps for Root Mean Square (RMS) and Maximum Absolute (MaxAbs) displacement metrics. These maps showed that lower-response TLCD configurations depend on both the fluid properties and the selected metric. The proposed methodology provides a tool for preliminary TLCD design studies based on explicit assumptions in fluid mechanics.

*Corresponding author: Magno de Oliveira Silva – E-mail: magno.silva@cefet-rj.br
[1]Centro Federal de Educação Tecnológica Celso Suckow da Fonseca (Cefet/RJ), Rio de Janeiro, RJ, Brazil – E-mail: magno.silva@cefet-rj.br, https://orcid.org/0000-0003-4625-560X
[2]Centro Federal de Educação Tecnológica Celso Suckow da Fonseca (Cefet/RJ), Centro de Interação Fluido-Estrutura e Acústica (CIFEA), Rio de Janeiro, RJ, Brazil – E-mail: julien.mauprivez@cefet-rj.br https://orcid.org/0000-0003-2734-4754
[3]Universidade Federal Rural do Rio de Janeiro (UFRRJ), Seropédica, RJ, Brazil – E-mail: felipeleite@ufrrj.br https://orcid.org/0000-0002-7090-5716
[4]Centro Federal de Educação Tecnológica Celso Suckow da Fonseca (Cefet/RJ), Centro de Interação Fluido-Estrutura e Acústica (CIFEA), Rio de Janeiro, RJ, Brazil – E-mail: bruno.cayres@cefet-rj.br https://orcid.org/0000-0002-0326-8462
[5]Centro Federal de Educação Tecnológica Celso Suckow da Fonseca (Cefet/RJ), Centro de Interação Fluido-Estrutura e Acústica (CIFEA), Rio de Janeiro, RJ, Brazil – E-mail: dadui.guerrieri@cefet-rj.br https://orcid.org/0000-0002-5088-5252

Keywords: vibration analysis, passive vibration control, tuned liquid column damper (TLCD), stochastic excitation, head-loss coefficient.

1 INTRODUCTION

The control of unwanted vibrations is essential in a wide range of applications, spanning civil engineering, mechanical systems, and aerospace industries. To mitigate these effects, dampers are widely employed as vibration control devices [33]. Among the various damper categories, passive devices stand out for their ability to dissipate energy without external power sources, achieving optimal performance when designed using systematic optimization criteria [1]. In this context, [18] conclude that passive Tuned Mass Dampers (TMDs) remain the predominant solution in industry, despite advancements in semi-active, active, and hybrid damping technologies. According to the authors, this predominance is due to the reliability and lower cost of passive dampers. More applications of TMD can be seen in [7, 9, 15].

Another solution, the Tuned Liquid Column Dampers (TLCDs), emerges as an effective alternative for vibration control. As explained by [17], these devices can adopt various configurations, utilizing fluid motion within a column to dissipate energy and exploiting resonance between the fluid and the primary structure. TLCDs have been widely used across diverse engineering fields due to their simple construction and efficient vibration attenuation. As noted in [16, 21], although TMDs generally offer superior control performance compared to TLCDs, the greater operational safety, lower installation and maintenance costs, and versatility of TLCDs make them a more viable option for many practical applications. Recent research has explored their use in mitigating earthquake-induced [8] and wind-induced vibrations [6, 39] in civil structures.

A key parameter for assessing TLCD performance is head loss, which directly influences the system's energy dissipation capacity. As discussed by [39], head loss is related to fluid viscosity and geometric characteristics of the TLCD, affecting the effective damping of the system. Therefore, accurately modeling head loss for fluids other than water is crucial for optimizing performance. Determining the exact damping characteristics of TLCDs remains a critical challenge in design. Unlike the mass and stiffness terms, which are geometrically defined, the damping term arises from complex fluid-structure interactions, including wall friction and flow separation at corners. Experimental studies by [12] demonstrated that the head loss coefficient is not a constant but depends on the flow regime and the geometry of the tube fittings. Similarly, [26] highlighted the discrepancies between classical laminar flow theories and experimental observations in U-tubes, proposing empirical corrections to account for the oscillating velocity profiles. Furthermore, investigations by [6] and [39] emphasize that establishing an equivalent damping coefficient for random vibration is non-trivial and essential for accurate response prediction. Consequently, relying solely on fixed experimental coefficients can lead to inaccuracies when fluid properties or scales change, thereby justifying the use of phenomenological models grounded in fundamental fluid mechanics.

In this study, a numerical model is developed to analyze the performance of a TLCD-coupled system under stochastic excitation, accounting for the effects of fluid type and viscosity on head loss. The equation of motion is numerically integrated using the Backward Differentiation Formula (BDF) method because the coupled system contains nonlinear damping terms and may become stiff for high-viscosity fluids. The specific contributions are: (i) dynamic evaluation of the head loss coefficient from the instantaneous Reynolds number, using Poiseuille and Swamee-Jain formulations; (ii) numerical comparison of water, ethylene glycol, SAE 30 oil, and glycerin in the same nominal TLCD geometry; and (iii) parametric performance maps in terms of effective column length and tube diameter.

This numerical work is related to the previous experimental investigation by [31], which used the same test bench to apply singular spectrum analysis (SSA) to vibration signals from a system with an attached TLCD. The present paper does not claim experimental validation of the damping model. Instead, selected physical parameters of that bench are used as input data for the numerical simulations, thereby keeping the computational study tied to a real laboratory configuration while focusing on the phenomenological treatment of head loss.

The remainder of this paper is organized as follows. Section 2 presents the structure–TLCD mathematical model, the head-loss formulation, and the numerical implementation. Section 3 discusses the time-history response, the influence of fluid properties, and the geometric parametric maps for Root Mean Square (RMS) and Maximum Absolute (MaxAbs) displacement. The final section summarizes the numerical findings, limitations, and implications for preliminary TLCD design.

2 MATERIALS AND METHODS

2.1 Equation of motion and physical setup

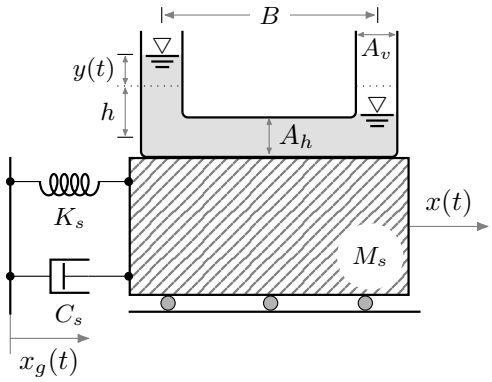
Analyzing the equations of motion for a TLCD-coupled system provides insight into the effects of this type of damper and supports the assessment of parameters that influence energy dissipation. Based on the work of [29] and in correlation with the research of [6], the equation of motion for a two-degree-of-freedom system, comprising a one-story building-like structure, here called the primary system, coupled with a TLCD, is given in Equation 2.1

$$\begin{bmatrix} M_s+\gamma A_v L & \gamma A_v \alpha L \\ \gamma A_v \alpha L & \gamma A_v L \end{bmatrix} \begin{Bmatrix} \ddot{x}(t) \\ \ddot{y}(t) \end{Bmatrix} + \begin{bmatrix} C_s & 0 \\ 0 & \frac{1}{2}\gamma A_v r_A \xi \mid \dot{y}(t) \mid \end{bmatrix} \begin{Bmatrix} \dot{x}(t) \\ \dot{y}(t) \end{Bmatrix}$$

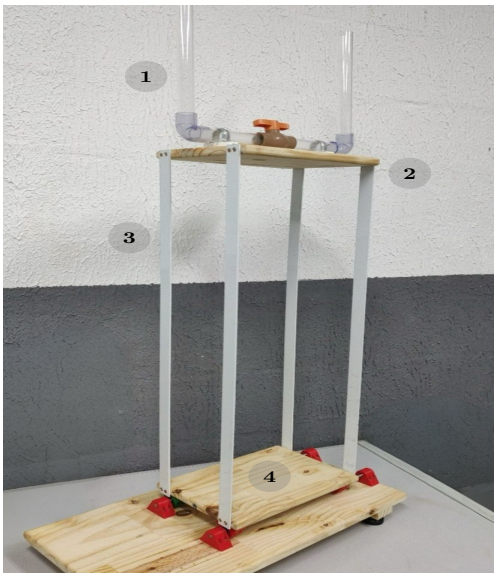
$$+ \begin{bmatrix} K_s & 0 \\ 0 & 2\gamma A_v g \end{bmatrix} \begin{Bmatrix} x(t) \\ y(t) \end{Bmatrix} \tag{2.1}$$

$$= - \begin{Bmatrix} M_s+\gamma A_v L \\ \gamma A_v \alpha L \end{Bmatrix} \ddot{x}_g(t),$$

where M_s represents the mass of the primary system, γ the fluid density, ξ the head-loss coefficient, and r_A the ratio between the cross-sectional areas of the vertical and horizontal sections of the TLCD, respectively denoted by A_v and A_h. The parameter α corresponds to the ratio between the tube width B and the effective length of the fluid $L = 2h + r_A B$, g is the gravitational constant, C_s is the damping coefficient of the primary system, and K_s is the stiffness of the system. Finally, $x(t)$ and $y(t)$ are, respectively, the relative displacement of the primary system and the displacement of the liquid in the vertical columns of the TLCD, and $\ddot{x}_g(t)$ is the ground acceleration. The system is illustrated in Figure 1(a).



(a)



(b)

Figure 1: (a) Simplified dynamic model of a single-degree-of-freedom system coupled with a TLCD, illustrating the vibratory system. (b) Experimental setup for testing, composed of: (1) TLCD, responsible for passive energy dissipation; (2) upper fixation platform; (3) aluminum flat bars supporting the structure; and (4) sliding base enabling the system's oscillatory motion.

Thus, the present work addresses the numerical solution of Equation 2.1, considering physical and geometric parameters associated with the bench shown in Figure 1(b). The problem formulation involves analyzing how TLCD parameters affect the system's dynamic response to assess vibration attenuation under stochastic excitation.

The test bench illustrated in Figure 1(b) has dimensions of $0.60 \times 0.30 \times 1.15$ m. Mass was added to the upper platform of the test bench by attaching steel weights. The technical characteristics of the bench are listed in Section 2.2.

2.2 Equation of motion matrices for the dynamic model with water

From Equation 2.1, the mass matrix (M) can be written as follows. The off-diagonal terms represent inertial coupling between the primary structure and the liquid column. Substituting the parameters from Table 1, we obtain the matrix M with its corresponding values

$$M = \begin{bmatrix} M_s + \gamma A_v L & \gamma A_v \alpha L \\ \gamma A_v \alpha L & \gamma A_v L \end{bmatrix} = \begin{bmatrix} 5.3533 & 0.1222 \\ 0.1222 & 0.2555 \end{bmatrix}.$$

To obtain the stiffness matrix (K), this work used the basic formula for the flexural stiffness of a beam, represented by the aluminum flat bar of the test bench (see Figure 1(b), item 3) in cantilever configuration [13], as shown in Equation 2.2

$$k = \frac{3EI}{\ell^3}, \tag{2.2}$$

where E is the material's modulus of elasticity, which for aluminum is typically around $69 \cdot 10^9$ Pa or 69 GPa, and I is the moment of inertia of the column's cross-section, and ℓ is the length of the beam. For a rectangle, $I = w \cdot z^3/12$, where w is the width, and z is the thickness of the beam. By substituting the values from Table 1, which provides further details on the beams, into Equation 2.2, and considering that the test bench has four parallel beams, the stiffness for the primary system is given by $K_s = 4.k = 143.5133$ N/m.

Regarding the fluid, the equivalent stiffness is derived from the conservative force resulting from the TLCD's gravitational potential energy, obtained using the expression $2\gamma A_v g$ in Equation 2.1. By substituting the appropriate values, we find 6.8481 N/m. Therefore, the stiffness matrix K for Equation 2.1 is given by

$$K = \begin{bmatrix} K_s & 0 \\ 0 & 2\gamma A_v g \end{bmatrix} = \begin{bmatrix} 143.5133 & 0 \\ 0 & 6.8481 \end{bmatrix}.$$

Damping is a more challenging property to determine theoretically as it depends on multiple factors, including internal material friction, boundary conditions, and interactions with other components of the system. Experimental methods are often used to determine damping factors, such as logarithmic decrement or frequency bandwidth [13]. Nonetheless, for this research, the formula $C_s = 2\beta\omega_n M_s$ is used to model the damping of the primary system, where ω_n is the natural angular frequency of the uncoupled primary system. This implies a simplified analytical approach [28].

The damping factor β is adopted as 2% for the equivalent SDOF model of the assembled primary structure [5]. This value is treated as a nominal effective damping ratio, intended to account for dissipation associated with the mounted aluminum bars, support conditions, and interface effects, rather than as an intrinsic property of aluminum alone [2, 3, 24, 30]. Since no dedicated modal identification or free-decay test was performed in the present study, this assumption is maintained as a practical modeling choice. The four bars are already represented in the equivalent structural

stiffness K_s. According to [4], the natural frequency f_n of the uncoupled primary SDOF system, in Hz, is given by Equation 2.3.

$$f_n = \frac{1}{2\pi}\sqrt{\frac{K_s}{M_s}}. \tag{2.3}$$

From the values already calculated for M_s and K_s, and making the substitutions in Equation 2.3, we obtain $f_n = 0.8444$ Hz and $\omega_n = 2\pi f_n = 5.3058$ rad/s. Then, $C_s = 2\beta\omega_n M_s = 1.0819$ Ns/m.

Thus, the damping matrix C in Equation 2.1, whose element at row 2, column 2 is obtained by substituting the corresponding values from Table 1, is given by

$$C = \begin{bmatrix} C_s & 0 \\ 0 & \frac{1}{2}\gamma A_v r_A \xi \mid \dot{y}(t) \mid \end{bmatrix} = \begin{bmatrix} 1.0819 & 0 \\ 0 & 0.1745\xi \mid \dot{y}(t) \mid \end{bmatrix}.$$

Table 1: Technical specifications and beam parameters of the test bench.

Component	Parameter	Value/Description
SDOF System	Mass (M_s)	5.0978 kg
	Stiffness (K_s)	143.5133 N/m
	Damping (C_s)	1.0819 Ns/m
	Natural frequency (f_n)	0.8444 Hz
TLCD	Cross-sectional areas (A_v, A_h)	0.00035 m^2
	Liquid density, water (γ)	998.2 kg/m^3
	Tube width (B)	0.35 m
	Initial liquid level (h)	0.1910 m
	Natural frequency	0.8240 Hz
Beams	Material	Aluminum
	Length (ℓ)	0.73 m
	Width (w)	0.0254 m
	Thickness (z)	0.00317 m

2.3 Estimation of the head loss coefficient

To investigate the influence of different fluid properties, the TLCD head-loss coefficient $\xi(t)$ is not treated as a constant experimental value. Instead, it is approximated analytically using principles of fluid mechanics, accounting for the fluid's viscosity, the tube roughness, and the instantaneous flow regime.

The total head loss coefficient ξ is defined as the sum of major losses (ξ_{major}), due to friction along the effective length of the liquid column, and minor losses (ξ_{minor}), caused by local singularities such as elbows and fittings. According to the Darcy-Weisbach formulation [22], $\xi(t)$ can be expressed as Equation 2.4

$$\xi(t) = \xi_{\text{major}}(t) + \xi_{\text{minor}} = f(t)\frac{L}{D} + \sum K_L, \tag{2.4}$$

where $f(t)$ is the Darcy friction factor, L is the effective length of the liquid, D is the internal diameter of the tube, and K_L represents the loss coefficients for the geometric singularities (e.g., 90° bends). In this experimental setup, the TLCD structure incorporates two standard 90° elbows. A constant loss coefficient of $K_L = 1.1$ was adopted for each elbow, consistent with typical values for standard bends found in fluid mechanics literature [22].

The friction factor $f(t)$ is a function of the dimensionless Reynolds number (Re) and the relative roughness of the pipe (ε/D). The Reynolds number, which represents a ratio between inertial and viscous effects in the fluid, is calculated based on the relative velocity of the fluid $\dot{y}(t)$ and on its kinematic viscosity ν, as expressed in Equation 2.5.

$$Re = \frac{|\dot{y}(t)|D}{\nu}. \tag{2.5}$$

The flow regime is classified as laminar for $Re < 2300$ and turbulent for $Re > 4000$. For the laminar steady regime, the friction factor depends only on the Reynolds number, following the theoretical derivation for Poiseuille flow [22], as given in Equation 2.6.

$$f = \frac{64}{Re} \quad \text{for} \quad Re < 2300. \tag{2.6}$$

In the transition and turbulent zones, determining the exact friction factor is complex. For numerical stability and simplicity, this study assumes that the turbulent formulation applies for all $Re \geq 2300$. Therefore, the Swamee-Jain equation [34], an explicit approximation of the Colebrook-White equation [22, 34], is employed as shown in Equation 2.7.

$$f = \frac{0.25}{\left[\log_{10}\left(\frac{\varepsilon}{3.7D} + \frac{5.74}{Re^{0.9}}\right)\right]^2} \quad \text{for} \quad Re \geq 2300. \tag{2.7}$$

This method provides a continuous assessment of the damping coefficient across the TLCD's entire operating range, approximating frictional losses in the transitional flow regime using a turbulent-flow characteristic curve.

In Equation 2.7, ε denotes the absolute roughness of the tube material. The internal surface of the TLCD is assumed to be hydraulically smooth, consistent with the acrylic tubes used in the experimental setup. For the numerical simulations, an absolute roughness of $\varepsilon = 1.5 \times 10^{-6}$ m was adopted, which corresponds to the standard specification for drawn tubing and smooth plastics in the Moody chart [23] and classic fluid mechanics literature [25, 37]. This parameter is also used to compute the relative roughness (ε/D) required to estimate the Darcy friction factor.

By implementing Equation 2.4 through Equation 2.7 into the numerical model, the damping term in the equation of motion adapts to the choice of fluid (via density γ and viscosity ν), the TLCD geometry (L and D), and the velocity $\dot{y}(t)$.

Although the fluid motion in a TLCD is oscillatory and exhibits entrance-length effects after the elbows, a quasi-steady-flow assumption is adopted in this study. This standard modeling approach implies that the instantaneous friction factor depends only on the instantaneous Reynolds

number, neglecting frequency-dependent effects on the velocity profile (such as the Womersley effect [38]) and entry length development.

It is discussed in [20] that this assumption has limitations in the context of liquid column oscillation, highlighting that it may lead to inaccuracies in predicting damping forces, especially at higher frequencies or for highly viscous fluids. For the specific case studied here, this assumption provides a reasonable approximation of the damping behavior.

2.4 Numerical method

The system of differential equations derived from Equation 2.1 was solved numerically in Python [27]. The `solve_ivp` function from the SciPy library [36] was employed for the time integration. Given the potential stiffness of the nonlinear coupled system equations, particularly when simulating high-viscosity fluids (e.g., glycerin), the BDF method was selected. This implicit multi-step method is commonly used for stiff problems and was adopted here to solve the transient response with variable time-stepping [35].

The implementation follows the standard BDF formulation for nonlinear problems, as detailed in [11, 19]. The main time-history and fluid-comparison simulations used $T = 60$ s, an output interval of 0.02 s, relative tolerance 10^{-7}, and absolute tolerance 10^{-10}. The parametric maps used the same total duration, with an output interval of 0.10 s, a relative tolerance of 10^{-5}, and an absolute tolerance of 10^{-8} to control computational cost. The geometric study first evaluated the original 11×11 grid and then used a nested 21×21 global grid, followed by local refinement around the lower-response grid points for the RMS and MaxAbs displacement metrics. Since the numerical response is evaluated at discrete time instants t_i, with $x_i = x(t_i)$ and $i = 1, \ldots, N$, these metrics are computed as

$$x_{\mathrm{RMS}} = \sqrt{\frac{1}{N}\sum_{i=1}^{N} x_i^2},$$

and

$$x_{\mathrm{MaxAbs}} = \max_{1 \le i \le N} |x_i|.$$

The excitation applied to the system is stochastic and modeled as a single reproducible random realization. The sliding base acceleration is generated as Equation 2.8

$$\ddot{x}_g(t) = A(t)\sin\Big(\Omega(t)\,t\Big), \tag{2.8}$$

where $A(t)$ is sampled from a normal distribution, $A(t) \sim \mathcal{N}(0,1)$, and $\Omega(t)$ is the angular frequency. A fixed random seed is used in the Python routine to ensure reproducibility; the reported RMS and MaxAbs values are therefore single-realization metrics rather than ensemble averages.

The angular frequency, $\Omega(t)$, is sampled from a Weibull distribution. This distribution ensures that the frequency values remain strictly positive, satisfying a physical requirement of the dy-

namical system. Accordingly, the parameters of the Weibull distribution are calibrated to yield a mean equal to the coupled natural frequency of the primary system, expressed as

$$\omega_s = \sqrt{\frac{K_s}{M_s + \gamma A_v L}}, \tag{2.9}$$

with a standard deviation of 0.25. This formulation explicitly accounts for the liquid mass contribution, thereby differing from Equation 2.3, which defines the uncoupled primary SDOF system.

This formulation keeps the sampled frequency positive while retaining fluctuations in both the amplitude and frequency of the ground acceleration.

The computational times reported in the grid-refinement comparison were obtained on a workstation equipped with an Intel(R) Core(TM) i5-9400 CPU at 2.90 GHz, 16.0 GB of RAM, and 6 logical CPU cores, running a 64-bit Windows 11 operating system. The simulations used Python 3.13.13 [27], NumPy 2.4.4 [10], SciPy 1.17.1 [36], and joblib 1.5.3 [14] for parallel execution.

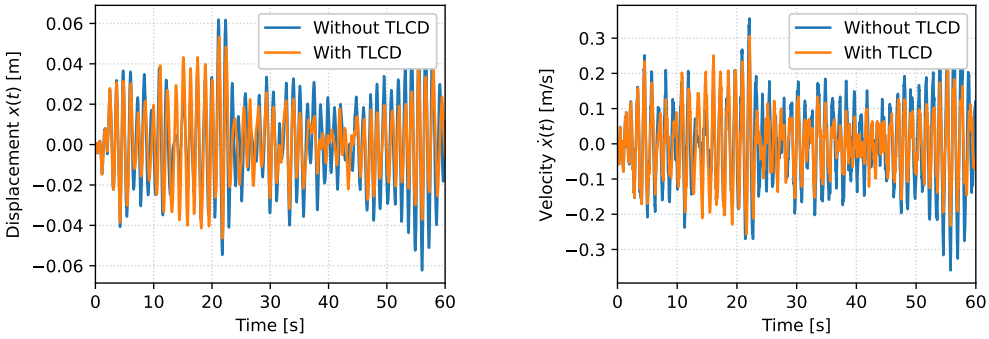
3 RESULTS

3.1 Time-history analysis

To assess TLCD efficiency, simulations were performed for two distinct configurations, with water as the liquid column. In the first configuration, the TLCD is considered inoperable (a closed valve impeding the liquid column's motion), resulting in an SDOF system with $y(t) = 0$ in Equation 2.1. In the second configuration, the TLCD operates normally, i.e., the 2-DOF system is solved. This comparison permits an objective quantification of the TLCD's efficiency in reducing the amplitude and velocity of the principal structure.

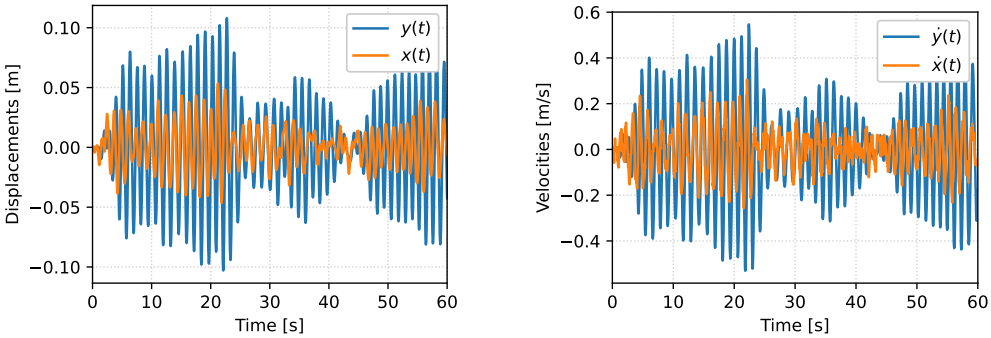
The simulated displacement $x(t)$ and velocity $\dot{x}(t)$ of the primary system for these two configurations are shown in Figure 2. The amplitudes of the displacement and velocity are reduced when the TLCD is operating. For this realization, the RMS displacement changed from 0.0224 m without TLCD to 0.0180 m with TLCD, corresponding to a reduction of 19.55%, while the MaxAbs displacement changed from 0.0627 m to 0.0533 m, corresponding to a reduction of 14.98%. These results suggest that vibration energy is partially transferred to the liquid column, with the device functioning as a passive damper in the simulated realization.

Now, considering the configuration with TLCD only, the displacement and velocity of the primary system and of the fluid free surface in the TLCD (i.e., the liquid-level displacement in the vertical columns) are shown in Figure 3. From Figure 3(a), it can be observed that the primary system $\big(x(t)\big)$ and the fluid free surface $\big(y(t)\big)$ exhibit distinct amplitudes over time, demonstrating that a portion of the vibrational energy is transferred to the TLCD. In general, $y(t)$ tends to reach higher values during certain intervals, due to the fluid absorbing and dissipating energy that would otherwise remain concentrated in the motion of the primary mass.



(a) (b)

Figure 2: (a) Time evolution of the primary system displacement $x(t)$ under random excitation, comparing the configuration without TLCD (blue line) and with TLCD (orange line). (b) Time evolution of the primary system velocity $\dot{x}(t)$ for the same random excitation, with and without TLCD.



(a) (b)

Figure 3: (a) Displacement response $x(t)$ of the primary system and $y(t)$ of the free surface of the fluid in the TLCD, under random excitation. (b) Corresponding velocities $\dot{x}(t)$ and $\dot{y}(t)$.

The velocities $\dot{x}(t)$ and $\dot{y}(t)$, shown in Figure 3(b), exhibit complementary oscillations, illustrating the energy transfer mechanism: when the structure starts to oscillate more intensely, the fluid responds with a different phase, reducing the velocity amplitude $\dot{x}(t)$. This nonlinear behavior of the damping, associated with the modulus of $\dot{y}(t)$, contributes to the limitation of the peak velocities of the primary structure in the simulated realization.

The time-history results in Figure 2 and Figure 3 show the same qualitative dynamic patterns reported in the preliminary RK45-based study by [32], that is, when the TLCD is active, the simulated displacement and velocity amplitudes of the primary structure are lower than in the con-

figuration without TLCD, and the liquid displacement $y(t)$ evolves with amplitudes and phase behavior distinct from the structural displacement $x(t)$. This agreement is qualitative and refers only to the observed response trends, namely attenuation of the primary-system motion and coupled structure–liquid interaction. A direct numerical comparison between RK45 and BDF is not performed because the present manuscript uses a revised dynamic head-loss formulation, different damping assumptions, and updated simulation settings.

3.2 Fluid viscosity influence

Using water as the reference case, other fluids are selected for similar numerical analyses, as described in Table 2. The physical properties of the fluids (density γ and kinematic viscosity ν) at a reference temperature of 20°C are set as per [22].

Table 2: Physical properties of the fluids considered in the numerical analysis at 20°C [22].

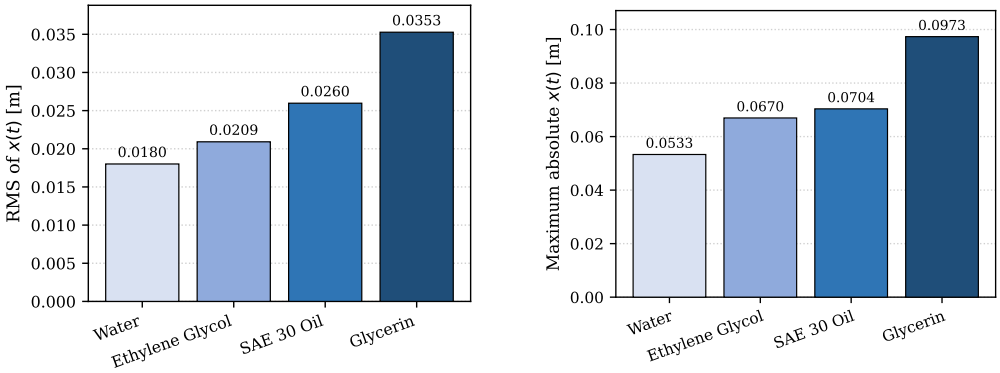
Fluid	**Density** γ [kg/m^3]	**Kinematic Viscosity** ν [m^2/s]
Water	998.2	1.004×10^{-6}
Ethylene Glycol	1115.0	1.890×10^{-5}
SAE 30 Oil	890.0	2.900×10^{-4}
Glycerin	1264.0	1.117×10^{-3}

The head-loss coefficient $\xi(t)$ is calculated based on the equations of Section 2.3, and the mean frequency and variance of the excitation are adjusted based on Equation 2.8 and Equation 2.9. The RMS and MaxAbs metrics defined in Section 2.4 are then obtained to compare the efficiency of each fluid in reducing the displacement amplitude of the structure.

The RMS displacement quantifies the energy content of the response over time, providing a measure of overall damping efficiency. The MaxAbs displacement informs the peak response amplitude of the structure. This metric is essential for evaluating the system's safety in ultimate limit states, ensuring that the TLCD effectively mitigates transient excursions.

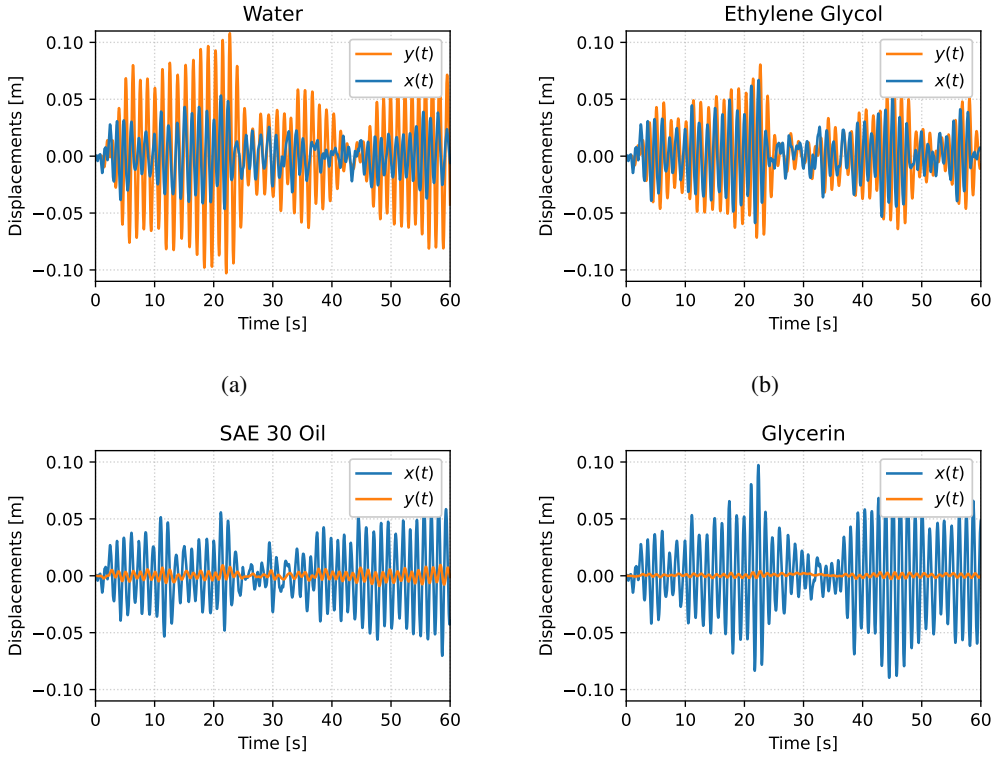
For water, the structure exhibited the lowest RMS and MaxAbs values in the nominal geometry, as shown in Figure 4. Replacing water with ethylene glycol, SAE 30 oil, or glycerin increased both metrics in this configuration. This trend is consistent with the increase in frictional resistance associated with viscosity, which restricts the liquid motion available for energy exchange between the structure and the TLCD. The coupled displacements shown in Figure 5 illustrate that the response also depends on the inertia and phase relation between $x(t)$ and $y(t)$.

SAE 30 oil and glycerin yielded higher structural vibration levels than water in the nominal small-diameter tube. These fluids have high $\xi(t)$ values, indicating greater frictional resistance to liquid motion. Figure 5(c) and (d) depict the displacements of the structure $x(t)$ and liquid $y(t)$ for oil and glycerin, respectively, showing that higher viscosity does not automatically improve the TLCD response in this nominal geometry.



(a) (b)

Figure 4: Fluids comparison of (a) RMS and (b) MaxAbs displacement with the original configuration of the experimental setup.



(a) (b)

(c) (d)

Figure 5: Displacements of the structure and fluids as a function of time for (a) water, (b) ethylene glycol, (c) SAE 30 oil, and (d) glycerin.

Table 3 summarizes the natural frequency of the system, RMS, and MaxAbs values of $x(t)$ for each fluid. These results indicate that fluid viscosity affects the dynamic response of the coupled system in the nominal geometry. While all fluids produce comparable natural frequencies, water provides the lowest RMS and MaxAbs response. Ethylene glycol and SAE 30 oil yield intermediate responses, while glycerin produces the largest RMS and peak displacement among the fluids considered.

Table 3: Comparison of TLCD performance with different fluids using the current geometric configuration ($L = 0.7320$ m, $D = 21.1$ mm).

Fluid	**Nat. Freq.** f_n [Hz]	x_{RMS} [m]	x_{MaxAbs} [m]
Water	0.8241	0.0180	0.0533
Ethylene Glycol	0.8218	0.0209	0.0670
SAE 30 Oil	0.8262	0.0260	0.0704
Glycerin	0.8189	0.0353	0.0973

3.3 Liquid column geometry parametric analysis

A refined parametric analysis is now performed on the TLCD geometry to identify regions of lower response for each fluid within the prescribed domain. The effective length $L = 2h + r_A B$, as defined in Section 2, and the diameter D are varied, and the resulting RMS and MaxAbs values are used as performance metrics. The liquid's effective length L is the main parameter responsible for tuning the liquid column frequency to the structure frequency, and D is associated with the tube cross-sectional area, influencing the head-loss factor, as discussed in Section 2.3.

The initial 11×11 grid was retained as a baseline case, and a nested 21×21 grid was subsequently employed to evaluate the sensitivity of the lower-response points to spatial discretization. Local refinements were then performed around the lower-response points obtained from the 21×21 grid, and the results were evaluated using the RMS and MaxAbs metrics. The identified configurations should be interpreted only as lower-response grid points within the simulated domain rather than continuous global optima.

Table 4 summarizes the grid-refinement comparison. The 21×21 grid increased the computational time by approximately a factor of 3.4 relative to the 11×11 grid for each fluid. The refined grid changed the selected lower-response region for several cases, including the RMS point for water, the MaxAbs point for water and ethylene glycol, and the RMS point for glycerin. For SAE 30 oil, both metrics selected the same points in the two grids. These results support the use of the refined grid and confirm that the configurations should be interpreted as lower-response grid points within the prescribed domain rather than as continuous optima.

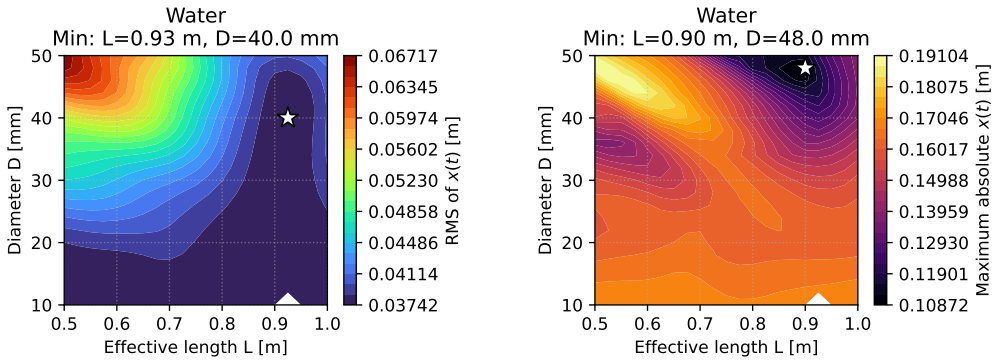
For water, as shown in Figure 6, the 21×21 RMS map gives $(L, D) = (0.925\text{ m}, 40.0\text{ mm})$, while the MaxAbs map gives $(L, D) = (0.900\text{ m}, 48.0\text{ mm})$. The subsequent local refinement

Table 4: Comparison between the original 11×11 grid and the nested 21×21 grid. Coordinate pairs are reported as $(L\ [\mathrm{m}], D\ [\mathrm{mm}])$, and Δ indicates the change in reduction relative to the nominal geometry.

Fluid	**Metric**	11×11 **point** (L,D)	21×21 **point** (L,D)	Δ **red.** [%]	t_{11} **[s]**	t_{21} **[s]**
Water	x_{RMS}	$(0.900, 22.0)$	$(0.925, 40.0)$	$+0.32$	83.9	289.3
	x_{MaxAbs}	$(0.900, 46.0)$	$(0.900, 48.0)$	$+1.41$		
Ethylene Glycol	x_{RMS}	$(0.500, 18.0)$	$(0.500, 18.0)$	$+0.00$	81.9	290.8
	x_{MaxAbs}	$(0.900, 34.0)$	$(0.925, 36.0)$	$+1.80$		
SAE 30 Oil	x_{RMS}	$(0.500, 10.0)$	$(0.500, 10.0)$	$+0.00$	79.3	280.8
	x_{MaxAbs}	$(0.500, 46.0)$	$(0.500, 46.0)$	$+0.00$		
Glycerin	x_{RMS}	$(0.500, 38.0)$	$(0.500, 40.0)$	$+0.48$	76.4	261.8
	x_{MaxAbs}	$(0.850, 10.0)$	$(0.850, 10.0)$	$+0.00$		

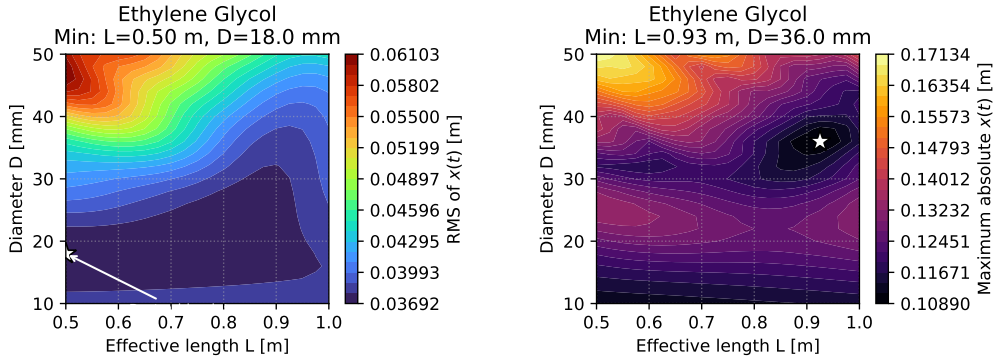
gave $(L,D) = (0.925\ \mathrm{m}, 40.8\ \mathrm{mm})$ for RMS and $(L,D) = (0.895\ \mathrm{m}, 47.2\ \mathrm{mm})$ for MaxAbs. These results indicate that larger diameters than the nominal value reduce the response of the water-filled TLCD within the explored range.

For ethylene glycol, the response maps shown in Figure 7 indicate a shallow RMS reduction and a stronger reduction in the peak response. The 21×21 grid points are $(L,D) = (0.500\ \mathrm{m}, 18.0\ \mathrm{mm})$ for RMS and $(L,D) = (0.925\ \mathrm{m}, 36.0\ \mathrm{mm})$ for MaxAbs. The local refinement gave $(L,D) = (0.5125\ \mathrm{m}, 17.6\ \mathrm{mm})$ for RMS and $(L,D) = (0.920\ \mathrm{m}, 36.8\ \mathrm{mm})$ for MaxAbs. The regions selected by the two metrics show that the design objective directly influences the preferred geometry.



(a) (b)

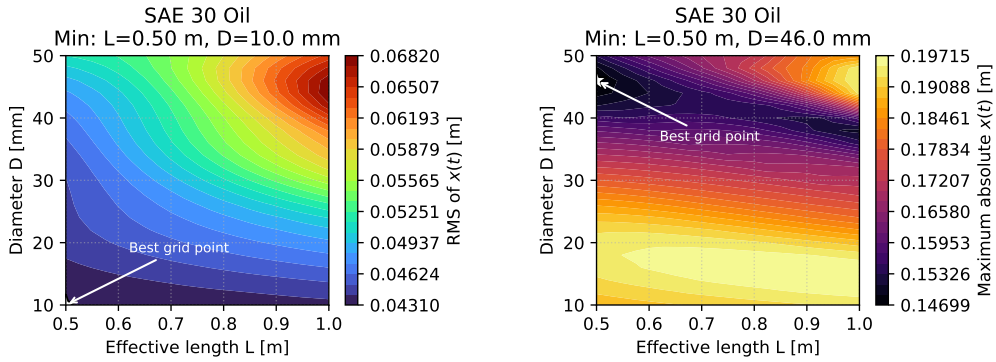
Figure 6: Refined 21×21 maps for water: (a) RMS of $x(t)$ with the lower-response grid point at $(L, D) = (0.925\,\mathrm{m}, 40.0\,\mathrm{mm})$ and (b) MaxAbs displacement of $x(t)$ with the lower-response grid point at $(L, D) = (0.900\,\mathrm{m}, 48.0\,\mathrm{mm})$.



(a) (b)

Figure 7: Refined 21×21 maps for ethylene glycol: (a) RMS of $x(t)$ with the lower-response grid point at $(L, D) = (0.500\,\text{m}, 18.0\,\text{mm})$ and (b) MaxAbs displacement of $x(t)$ with the lower-response grid point at $(L, D) = (0.925\,\text{m}, 36.0\,\text{mm})$.

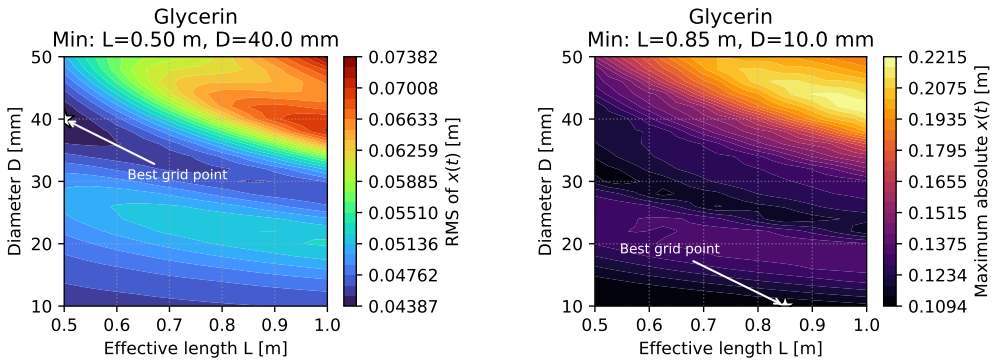
The results for viscous fluids illustrate that the TLCD geometry must be adjusted before drawing conclusions about their damping performance. For SAE 30 oil, the 21×21 grid retained the same lower-response points obtained with the coarser grid: $(L, D) = (0.500\ \text{m}, 10.0\ \text{mm})$ for RMS and $(L, D) = (0.500\ \text{m}, 46.0\ \text{mm})$ for MaxAbs, as shown in Figure 8. The local refinement retained both values. The difference between the RMS and MaxAbs regions reflects the competing effects of fluid inertia, tuning length, and frictional loss represented by the head-loss formulation in Equation 2.4 through Equation 2.7.



(a) (b)

Figure 8: Refined 21×21 maps for SAE 30 oil: (a) RMS of $x(t)$ with the lower-response grid point at $(L, D) = (0.500\,\text{m}, 10.0\,\text{mm})$ and (b) MaxAbs displacement of $x(t)$ with the lower-response grid point at $(L, D) = (0.500\,\text{m}, 46.0\,\text{mm})$.

Figure 9 gives the response maps for glycerin. The 21×21 RMS metric selects $(L,D) = (0.500\,\text{m}, 40.0\,\text{mm})$, whereas the MaxAbs metric selects $(L,D) = (0.850\,\text{m}, 10.0\,\text{mm})$. The local refinement gave $(L,D) = (0.500\,\text{m}, 39.6\,\text{mm})$ for RMS and $(L,D) = (0.825\,\text{m}, 10.2\,\text{mm})$ for MaxAbs. This metric dependence indicates that the high density and viscosity of glycerin alter both the inertial coupling and the frictional dissipation, so a single geometric recommendation cannot be made without defining the design objective.



(a) (b)

Figure 9: Refined 21×21 maps for glycerin: (a) RMS of $x(t)$ with the lower-response grid point at $(L, D) = (0.500\,\text{m}, 40.0\,\text{mm})$ and (b) MaxAbs displacement of $x(t)$ with the lower-response grid point at $(L, D) = (0.850\,\text{m}, 10.0\,\text{mm})$.

Table 5 summarizes the reduction of RMS and MaxAbs values of the displacement $x(t)$ after the local refinements around the 21×21 lower-response grid points, using the nominal geometry as the reference case under the same parametric-study simulation settings. The total computational time for the grid-comparison and local-refinement procedure was 2094.2 s.

Table 5: Locally refined lower-response points and percentage reduction in the structural response compared with the nominal geometric configuration under the same parametric-study settings.

Fluid	$\boldsymbol{x}_{\text{RMS}}$ **point** $(L\ [\text{m}], D\ [\text{mm}])$	$\boldsymbol{x}_{\text{RMS}}$ **red. [%]**	$\boldsymbol{x}_{\text{MaxAbs}}$ **point** $(L\ [\text{m}], D\ [\text{mm}])$	$\boldsymbol{x}_{\text{MaxAbs}}$ **red. [%]**
Water	$(0.925, 40.8)$	4.15	$(0.895, 47.2)$	34.23
Ethylene Glycol	$(0.5125, 17.6)$	0.71	$(0.920, 36.8)$	16.11
SAE 30 Oil	$(0.500, 10.0)$	7.51	$(0.500, 46.0)$	23.61
Glycerin	$(0.500, 39.6)$	14.85	$(0.825, 10.2)$	18.49

4 CONCLUSIONS AND FUTURE WORKS

This study presented a numerical framework for analyzing the performance of Tuned Liquid Column Dampers (TLCDs). A numerical approach based on the implicit, variable-order multi-step BDF method was used to simulate the dynamic behavior of the structural system coupled with the TLCD, accounting for nonlinear damping and stochastic excitation. By implementing a dynamic evaluation of the head-loss coefficient using the Darcy-Weisbach, Poiseuille, and Swamee-Jain formulations, the model captured the influence of fluid viscosity on the system's damping response.

The comparative analysis showed that simply substituting water with higher-viscosity fluids in the nominal small-diameter configuration ($D = 21.1$ mm) increased the simulated structural response for both RMS and MaxAbs metrics. The refined parametric maps indicated that geometric adjustment can reduce RMS and peak displacement for all fluids within the analyzed domain, with reductions ranging from 0.71% to 14.85% for RMS and from 16.11% to 34.23% for MaxAbs after local refinement. The lower-response points were metric-dependent, and the grid-refinement comparison showed that the coarser grid could select different regions for some cases. Therefore, viscous fluids should not be treated as generally superior or inferior; their effectiveness depends on the TLCD geometry and on the selected design metric.

The main limitations of the present study are its numerical character, the use of physical bench parameters without quantitative experimental validation of the present damping model, the single-realization stochastic excitation, and the restriction of the conclusions to the analyzed fluids and the prescribed ranges of L and D. Future work should prioritize targeted experimental calibration of the head-loss model, direct measurement of the liquid displacement $y(t)$, and model-comparison studies following comparison of the numerical model with measured responses.

Acknowledgments

M.O. Silva thanks the financial and institutional support of the Federal Center for Technological Education Celso Suckow da Fonseca (Cefet/RJ). F. L. C. Silva acknowledges financial support from the CNPq grant "bolsa de produtividade PQ-C" 312646/2025-9. J.O. Mauprivez, B.C. Cayres and D. C. Guerrieri gratefully acknowledge the support provided by the Financier of Studies and Projects (FINEP) to the Centro de Interação Fluido-Estrutura e Acústica (CIFEA) project, under grant Ref. 1038.25.

Data availability

Do not apply.

Associate editor: Antônio José Silva Neto

REFERENCES

[1] A.K. Agrawal & J.N. Yang. Design of passive energy dissipation systems based on lqr control methods. *Journal of Intelligent Material Systems and Structures*, **10**(12) (1999), 933–944. doi:10.1106/fb58-n1dg-ecjt-b8h4.

[2] ASTM International. ASTM E756-05(2010): Standard Test Method for Measuring Vibration-Damping Properties of Materials (2010). doi:10.1520/E0756-05R10. URL `https://store.astm.org/e0756-05r10.html`.

[3] ASTM International. ASTM E1876-22: Standard Test Method for Dynamic Young's Modulus, Shear Modulus, and Poisson's Ratio by Impulse Excitation of Vibration (2022). doi:10.1520/E1876-22. URL `https://store.astm.org/e1876-22.html`.

[4] A. Brandt. "Noise and vibration analysis: signal analysis and experimental procedures". Wiley, Hoboken, NJ, 2nd ed. (2023). doi:10.1002/9781118962176. Includes bibliographical references and index.

[5] A.K. Chopra. "Dynamics of structures". Prentice-Hall international series in civil engineering and engineering mechanics. Prentice Hall, Upper Saddle River, N.J (1995).

[6] A. Di Matteo, F. Lo Iacono, G. Navarra & A. Pirrotta. Direct evaluation of the equivalent linear damping for TLCD systems in random vibration for pre-design purposes. *International Journal of Non-Linear Mechanics*, **63** (2014), 19–30. doi:10.1016/j.ijnonlinmec.2014.03.009.

[7] S. Elias & V. Matsagar. Research developments in vibration control of structures using passive tuned mass dampers. *Annual Reviews in Control*, **44** (2017), 129–156. doi:10.1016/j.arcontrol.2017.09.015.

[8] M. Fahimi Farzam, M. Charkhtab Basim & R. Maroofiazar. Efficiency and robustness of optimally designed tuned mass dampers for mid-and high-rise buildings under far and near-field earthquakes. *Journal of Vibration Engineering & Technologies*, **11**(2) (2022), 699–719. doi:10.1007/s42417-022-00604-x.

[9] J.A. Guimarães, M. Farias, M. Braz-César & R. Barros. Dynamic analysis of wind tower and dimensioning of tuned mass damper. *Revista de Engenharia e Pesquisa Aplicada*, (2021). doi:10.25286/repa.v6i2.1465. URL `http://revistas.poli.br/index.php/repa/article/view/1465`.

[10] C.R. Harris, K.J. Millman, S.J. van der Walt, R. Gommers, P. Virtanen, D. Cournapeau, E. Wieser, J. Taylor, S. Berg, N.J. Smith *et al.* Array programming with NumPy. *Nature*, **585** (2020), 357–362. doi:10.1038/s41586-020-2649-2.

[11] A.C. Hindmarsh, P.N. Brown, K.E. Grant, S.L. Lee, R. Serban, D.E. Shumaker & C.S. Woodward. SUNDIALS: Suite of nonlinear and differential/algebraic equation solvers. *ACM Transactions on Mathematical Software*, **31**(3) (2005), 363–396. doi:10.1145/1089014.1089020.

[12] P. Hitchcock, K. Kwok, R. Watkins & B. Samali. Characteristics of liquid column vibration absorbers (LCVA)—I. *Engineering Structures*, **19**(2) (1997), 126–134. doi:10.1016/s0141-0296(96)00042-9.

[13] D.J. Inman. "Engineering vibration". Always Learning. Pearson, Boston, Mass., 4th ed. (2014). Internat. ed.

[14] T. joblib developers. joblib (2025). doi:10.5281/zenodo.17936197.

[15] A.M. Kaynia, D. Veneziano & J.M. Biggs. Seismic effectiveness of tuned mass dampers. *Journal of the Structural Division*, **107**(8) (1981), 1465–1484. doi:10.1061/jsdeag.0005760.

[16] N. Khodaie. Parametric study of wind-induced vibration control of tall buildings using TMD and TLCD systems. *Structures*, **57** (2023), 105126. doi:10.1016/j.istruc.2023.105126.

[17] T. Konar & A.D. Ghosh. A review on various configurations of the passive tuned liquid damper. *Journal of Vibration and Control*, **29**(9–10) (2022), 1945–1980. doi:10.1177/10775463221074077.

[18] L. Koutsoloukas, N. Nikitas & P. Aristidou. Passive, semi-active, active and hybrid mass dampers: A literature review with associated applications on building-like structures. *Developments in the Built Environment*, **12** (2022), 100094. doi:10.1016/j.dibe.2022.100094.

[19] Lawrence Livermore National Laboratory. BDF Method - SUNDIALS Wiki (2024). URL `http://sundials.wikidot.com/bdf-method`. Accessed: 2025-11-20.

[20] E.A. Martínez-Padilla, A. Arrieta-Pastrana, O.E. Coronado-Hernández, M. Saba & V.S. Fuertes-Miquel. Predictive Analysis for U-Tube Transient Flow Events: A Digitalisation Framework. *Fluids*, **10**(9) (2025), 247. doi:10.3390/fluids10090247.

[21] C. Masnata, A. Di Matteo, C. Adam & A. Pirrotta. Sliding TLCD for vibration control of base-isolation systems: experimental comparison with traditional TLCD and TMD. *Journal of Physics: Conference Series*, **2647**(17) (2024), 172005. doi:10.1088/1742-6596/2647/17/172005.

[22] J.W. Mitchell. "Fox and McDonald's introduction to fluid mechanics". Wiley, Hoboken, 10th ed. (2020). EMEA edition. Includes bibliographical references and index.

[23] L.F. Moody. Friction factors for pipe flow. *Journal of Fluids Engineering*, **66**(8) (1944), 671–678. doi:10.1115/1.4018140.

[24] F. Müller, L. Woiwode, J. Gross, M. Scheel & M. Krack. Nonlinear damping quantification from phase-resonant tests under base excitation. *Mechanical Systems and Signal Processing*, **177** (2022), 109170. doi:10.1016/j.ymssp.2022.109170.

[25] B.R. Munson, T.H. Okiishi, W.W. Huebsch & A.P. Rothmayer. "Fundamentals of fluid mechanics". Wiley, Hoboken, NJ, 7th ed. (2013). Includes indexes.

[26] A. Ogawa, S. Tokiwa, M. Mutou, K. Mogi, T. Sugawara, M. Watanabe, K. Satou, T. Kikawada, K. Shishido & N. Matumoto. Damped oscillation of liquid column in vertical U-tube for Newtonian and non-Newtonian liquids. *Journal of Thermal Science*, **16**(4) (2007), 289–300. doi:10.1007/s11630-007-0289-6.

[27] Python Software Foundation. "Python 3.13 Documentation" (2026). URL `https://docs.python.org/3.13/`.

[28] S.S. Rao. "Mechanical vibrations". Pearson Deutschland, Harlow, United Kingdom (2018), 632 p. URL `https://elibrary.pearson.de/book/99.150005/9781292178615`. Sixth edition in SI Units, global edition. Authorized adaptation from the United States sixth edition, 2017. ISBN 978-0-134-36130-7.

[29] F. Sadek, B. Mohraz & H.S. Lew. Single-and multiple-tuned liquid column dampers for seismic applications. *Earthquake Engineering & Structural Dynamics*, **27**(5) (1998), 439–463. doi:10.1002/(sici)1096-9845(199805)27:5⟨439::aid-eqe730⟩3.0.co;2-8.

[30] M. Scheel, T. Weigele & M. Krack. Challenging an experimental nonlinear modal analysis method with a new strongly friction-damped structure. *Journal of Sound and Vibration*, **485** (2020), 115580. doi:10.1016/j.jsv.2020.115580.

[31] M.d.O. Silva, B.C. Cayres & F.L.C.d. Silva. Enhancing vibration analysis with singular spectrum analysis in a system with passive damper attached. *Journal of the Brazilian Society of Mechanical Sciences and Engineering*, **47** (2025), 138. doi:10.1007/s40430-025-05443-x.

[32] M.O. Silva, B.C. Cayres, J.O. Mauprivez, D.C. Guerrieri & F.L.C.d. Silva. Análise e Solução Numérica de um Sistema com Controle Passivo de Vibrações Sob Excitação Estocástica. *Proceeding Series of the Brazilian Society of Computational and Applied Mathematics*, **12**(1) (2026). doi: 10.5540/03.2026.012.01.0251. Trabalho apresentado no XLIV CNMAC, Fundação Getulio Vargas, Rio de Janeiro, RJ, 2025.

[33] M.H. Stanikzai, S. Elias & Y. Chae. Recent advances in hybrid vibration-control systems. *Practice Periodical on Structural Design and Construction*, **27**(3) (2022), 03122003. doi:10.1061/(asce)sc.1943-5576.0000685.

[34] P.K. Swamee & A.K. Jain. Explicit equations for pipe-flow problems. *Journal of the Hydraulics Division*, **102**(5) (1976), 657–664. doi:10.1061/jyceaj.0004542.

[35] The SciPy Community. Integration and ODEs (scipy.integrate) (2024). URL `https://docs.scipy.org/doc/scipy/reference/integrate.html`. Accessed: 2024-02-27.

[36] P. Virtanen, R. Gommers, T.E. Oliphant, M. Haberland, T. Reddy, D. Cournapeau, E. Burovski, P. Peterson, W. Weckesser, J. Bright *et al.* SciPy 1.0: fundamental algorithms for scientific computing in Python. *Nature Methods*, **17**(3) (2020), 261–272. doi:10.1038/s41592-019-0686-2.

[37] F.M. White. “Fluid Mechanics”. McGraw-Hill, New York, NY, 8th ed. (2016). Includes index and references.

[38] J. Womersley. XXIV. Oscillatory motion of a viscous liquid in a thin-walled elastic tube—I: The linear approximation for long waves. *The London, Edinburgh, and Dublin Philosophical Magazine and Journal of Science*, **46**(373) (1955), 199–221. doi:10.1080/14786440208520564.

[39] J.C. Wu, M.H. Shih, Y.Y. Lin & Y.C. Shen. Design guidelines for tuned liquid column damper for structures responding to wind. *Engineering Structures*, **27**(13) (2005), 1893–1905. doi:10.1016/j.engstruct.2005.05.009.

How to cite

M.O. Silva, J.O. Mauprivez, F.L.C. Silva, B.C. Cayres & D.C. Guerrieri. Tuned Liquid Column Dampers under Stochastic Excitation with Viscosity and Geometric Effects. *Trends in Computational and Applied Mathematics*, **27**(2026), e01901. doi: 10.5540/tcam.2026.027.e01901.

CC BY